J. Synchrotron Rad. (2000). **7**, 81–88

Parametric down conversion of X-ray photons

Bernhard Adams,[a]* Patricia Fernandez,[b] Wah-Keat Lee,[b] Gerhard Materlik,[a] Dennis M. Mills[b] and Dmitri V. Novikov[a]

[a]Hamburger Synchrotronstrahlungslabor HASYLAB am Deutschen Elektronen-Synchrotron DESY, Notkestrasse 85, 22603 Hamburg, Germany, and [b]Advanced Photon Source, Argonne National Laboratory, Argonne, IL, USA. E-mail: adams@x4u2.desy.de

(*Received 20 April 1999; accepted 23 November 1999*)

Parametric down conversion of X-ray photons in diamond crystals was detected in two experiments, both using the phase-matching scheme first employed in the X-ray regime by Eisenberger & McCall [*Phys. Rev. Lett.* (1971), **26**, 684–688]. The conversion events were detected by a combination of time-correlation spectroscopy and energy discrimination, using Si drift-chamber detectors. The time-correlation spectra give a direct comparison of the conversion rate over the accidental coincidence rate. Mechanisms for possible detection of false events and ways to cross check against them are discussed in detail.

Keywords: non-linear X-ray optics; parametric down conversion.

1. Introduction

The effect of parametric down conversion (PDC) is the spontaneous decay of a photon of frequency ω_p into two of frequencies ω_i and ω_s in an optically non-linear medium. Due to energy conservation, $\omega_p = \omega_i + \omega_s$. The indices p, i and s have historic origin and denote 'pump', 'idler' and 'signal', respectively. Just as with spontaneous emission of radiation, there is no classical explanation for this effect. Semiclassically, PDC can be described as frequency mixing of a vacuum fluctuation of frequency ω_i with a real photon of frequency ω_p, producing photons at ω_i and the beat frequency ω_s. Generation of the sum frequency $\omega_p + \omega_i$ is forbidden by energy conservation. Just as in optical sum and difference frequency generation, the exiting intensity is proportional to the product of the incident intensities, the event rate of PDC is proportional to the incident intensity at ω_p times the power density of vacuum fluctuations at ω_i. The latter being much higher for X-ray frequencies than in the visible regime, detectable event rates for PDC can be expected even in the exceedingly weak optical non-linearities which are typical for the X-ray regime. With the power density of vacuum fluctuations being beyond human control, the event rate of PDC depends linearly on the incident intensity.

The effect of PDC is well known in the visible-light regime and is used for a variety of applications, such as tests of the interpretation of quantum theory (Bell's inequality) (Kwiat, Steinberg & Chiao, 1993; Rarity & Tapster, 1990), two-photon interferometry (Hong *et al.*, 1987; Ou & Mandel, 1988) and possibly communications technology. The two converted photons exit the non-linear dielectric almost simultaneously to within their temporal coherence times (Friberg *et al.*, 1985).

The wavefunction of the two photons generated by PDC is not just a product of two single-photon wavefunctions but rather a so-called entangled state. This leads to highly non-classical correlations, such as demonstrated by Brendel *et al.* (1991), and to non-local phenomena, *i.e.* the way a measurement is performed on one photon affects the probabilities of measurement results on the other photon.

After theoretical predictions by Freund & Levine (1969), Eisenberger & McCall (1971) first demonstrated the effect of PDC in the X-ray regime (henceforth XPDC) on an X-ray tube. This reflects the linear (instead of square) dependency of PDC on the incident intensity. More recently, Yoda *et al.* (1998) reported XPDC with synchrotron radiation.

2. Theory

PDC requires a dielectric with a non-linear electrical susceptibility within which sum and difference frequencies can be generated. For a sample with absorption edges far below the X-ray photon energies, this non-linearity can be calculated by classical electrodynamics (Freund & Levine, 1969; Eisenberger & McCall, 1971) in the approximation of free electrons. By incorporating the power density of vacuum fluctuations (see Appendix *A*), the conversion cross section is found to be of the order of

$$\frac{\mathrm{d}\sigma}{\mathrm{d}\Omega} = \gamma^2 \frac{137}{4\pi} r_e^4 k_p^2 \, \mathrm{d}x, \qquad (1)$$

where γ is a geometry factor of the order of unity, $\mathrm{d}x = \mathrm{d}\omega/\omega$ is the relative energy bandwidth, r_e is the classical electron radius and $k_p = \omega_p/c$. For a 1% energy bandwidth of the converted photons and 20 keV incident energy, this is roughly 10^{-9} of the Thomson scattering cross section.

In order to direct the converted photons into well defined beams, a phase-matching condition must be fulfilled: $\mathbf{k}_p + \mathbf{H} = \mathbf{k}_i + \mathbf{k}_s$, where $\mathbf{k}$ denotes the wave vectors of the photons and $\mathbf{H}$ is a crystal momentum vector. We denote $\mathbf{k}_p + \mathbf{H}$ by $\mathbf{k}_H$. Owing to the dispersion of the refractive index in the X-ray regime, phase matching in XPDC due to the non-linearity of free electrons is impossible for $\mathbf{H} = 0$.

In the phase-matching scheme proposed by Freund & Levine (1969), a crystal is detuned slightly away from the Bragg condition for the incident beam $(\omega_p, \mathbf{k}_p)$ so that $|\mathbf{k}_H| < |\mathbf{k}_i| + |\mathbf{k}_s|$. Then, $\mathbf{k}_i$ and $\mathbf{k}_s$ form non-vanishing angles α_i and α_s of opposite sign relative to $\mathbf{k}_H$; and $\mathbf{k}_H$, $\mathbf{k}_i$ and $\mathbf{k}_s$ are all coplanar. Since this condition has rotational symmetry about $\mathbf{k}_H$, then $\mathbf{k}_i$ and $\mathbf{k}_s$ lie anywhere (but coplanar) on cones with apex angles given by α_i and α_s, respectively, and centred around $\mathbf{k}_H$. A sketch of this geometry in reciprocal space is shown in Fig. 1. A simple calculation on the basis of kinematical scattering theory gives the detuning angle $\Delta\Theta$ for $\alpha_i = \alpha_s$ (*i.e.* $|\mathbf{k}_i| = |\mathbf{k}_s|$) to be

$$\Delta\Theta = (\alpha_s^2/2 + 3\chi_0)/\sin 2\Theta + \chi_0/\tan\Theta, \qquad (2)$$

where χ_0 is the linear electric susceptibility of the sample material. The term $\alpha_s^2/(2\sin 2\Theta)$ has a simple geometric origin which is evident from Fig. 1, $3\chi_0/\sin 2\Theta$ is due to the dispersion of the refractive index and $\chi_0/\tan\Theta$ is an additional refraction correction which appears for the Bragg but not the Laue case for the incident beam.

3. Experimental considerations

Conversion events can be detected by energy analysis of the detected photons and by recording coincidences between the two detectors, possibly in combination. Owing to the low conversion cross section, special care has to be taken to distinguish the conversion signal from statistical background and electronic noise.

The statistical background is caused by any two photons hitting the two detectors simultaneously to within their and the coincidence circuitry's time resolution and being passed as having the correct energies by the energy analysis circuitry (if any). It is proportional to the temporal average of the product of the momentary signal output rates of the two signal chains. These depend very much on details of time structure of the source intensity and of the detector and signal chain time resolution. Generally speaking, the statistical event rate is proportional to the square of the incident intensity and is roughly inversely proportional to a typical time constant τ of the source intensity or the time resolution ρ of the detectors and the coincidence circuitry, whichever is larger.

Obviously, the statistical event rate is reduced as the time resolution of the detectors is improved, down to the limit of the source time structure. With X-ray photon detectors, there is always a trade-off between time and energy resolution and the optimum choice of detectors depends on the source.

Although, in principle, the statistical coincidence rate can be calculated, this is very difficult to do in practice and the statistical event rate should be determined empirically. The best way of doing this is to record time-correlation spectra. Coincidence should appear at zero time difference as a peak above the background of statistical correlations, showing the temporal autocorrelation of the source intensity. This autocorrelation also has a peak at zero time difference and has the period τ of the source intensity. In order to discern the true coincidence peak from the one due to statistical coincidences, the time-correlation spectra should cover several periods τ.

The ubiquitous electronic noise in synchrotron radiation laboratories may couple into both signal chains and produce fake coincidences. With the low event rates to be expected, even rarely and irregularly (*i.e.* hard to eliminate) occurring stray signals can be a problem. It is therefore imperative to cross check against this possibility. One obvious way is to scan the detuning angle $\Delta\Theta$. Since the two photons in a conversion event and the Bragg reflected beam are coplanar, another way of checking for false events is to move the detectors away from the Bragg reflected beam such that no plane containing the Bragg reflected beam intersects both detector entrance windows. It is also a good idea to insert an analog delay (such as a length of coaxial cable) into one of the signal chains. This shifts the true point of zero time difference in the time-correlation spectrum while electronic noise coupled into the signal chains at any point after the delay appears at the nominal zero position.

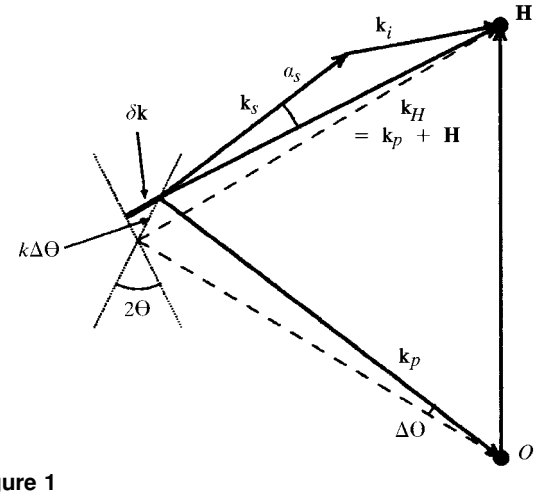

Figure 1
Phase matching scheme.

4. Experiment

The present experiments were performed at the undulator beamline ID18 (Rüffer & Chumakov, 1996) of the ESRF and the bending-magnet beamline 1BM of the APS. Phase matching was performed by use of diamond crystals of (100) and (111) orientation in the manner described above. Our detectors were Si drift chambers made by Röntec

GmbH (Berlin, Germany; http://www.roentec.de) with an energy resolution of ∼300 eV (see *Discussion* below) and a time resolution of ∼100 ns. Their active areas are circular with diameters of 2.1 mm. From the output of each detector a prompt signal (containing the timing information) and an energy signal (through a single channel analyser) were derived. These signals were fed into a time-to-digital converter, implemented in programmable logic (Adams, 1999), which recorded time-correlation spectra of detector events in the energy ranges defined by the single channel analysers whose times of occurrence were derived from the prompt signals. The time resolution of the data is 10 ns over a range of ±10 µs, the sign referring to which of the detectors recorded the first photon of a specific correlation event. Fig. 2 shows the scattering geometry with numerical values from the ESRF experiment. Details are listed below.

At ID18 of the ESRF, an Si(111) double-crystal monochromator, set to 14.4 keV, delivered a flux of $\sim 1.5 \times 10^{10}$ photons s^{-1} through an attenuator with 10% transmission and slits of size 0.2 mm × 0.2mm. This beam was incident on a diamond plate of thickness 0.5 mm, adjusted to a symmetrical (400) Bragg reflex. In order to reduce the background signal it was mounted such that the direct beam would pass through without hitting any obstacle. The attenuation improved the signal-to-background ratio because the signal strength is proportional to the incident intensity while the statistical background varies as its square. At the time of the experiment the ESRF was operating in the two-thirds filling mode (*i.e.* every bucket in two-thirds of the ring being filled and the remaining third empty).

The detectors were arranged within the scattering plane (containing $\mathbf{k}_p$ and $\mathbf{k}_H$) at a distance of 850 mm from the sample with a spacing of the entrance windows of ±20 mm symmetrically to the Bragg reflected beam. This defined $\alpha_i = \alpha_s = 1.37°$. Air absorption and scattering of the Bragg reflected beam were minimized by flowing He through a beam pipe, leaving only 50 mm of air path after the sample.

The rocking width of the sample diamond was $\sim 5 \times 10^{-3}$ deg (with a small satellite peak, see Fig. 3). Since the divergence of the undulator beam, further cut down by the small slits, was only ∼5 µrad in the scattering plane, Bragg angle dispersion between the monochromator and the sample gives almost no contribution to the rocking width.

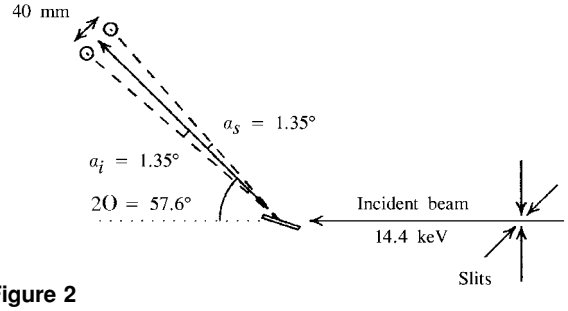

Figure 2
Scattering geometry. The sample-to-detectors distance is 850 mm and the slits are 0.2 mm × 0.2 mm.

Since the second experiment was performed at a bending-magnet station of the APS, we had to take care to match the wavelength dispersion of the monochromator and the sample. Our choice was an Si(220) double-crystal monochromator in conjunction with a (111) diamond reflex. The beamline optics were (going downstream): a plane mirror, the double-crystal monochromator with sagittally focusing second crystal, and another mirror which was capable of vertical focusing but was made flat so as not to spoil the dispersion matching of monochromator and sample. The monochromator was set to 18.6 keV and delivered a flux on the sample of $\sim 1.5 \times 10^9$ photons s^{-1} through a slit of width 5 mm and height 1 mm. This, integrated over the beam size, is ten times less than at ESRF-ID18, resulting in a tenfold lower conversion rate because of the linear dependence on the incident intensity.

At the time of the experiment the APS was operating in the 6+22*1 mode, meaning that ∼10% of the total ring current was in six subsequent buckets, then 200 ns of empty buckets, then 22 single buckets at 150 ns mutual spacing containing the rest of the current. Two Si drift chambers were placed at a distance of 1310 mm from the sample with a spacing of ±24 mm from the Bragg reflected beam such that the line joining the two entrance windows was orthogonal to the scattering plane. A pair of avalanche photodiodes, each of active area 10 mm × 10 mm, was put into the scattering plane at the same distance and mutual spacing. Thus, for both pairs of detectors we had $\alpha_i = \alpha_s = 1°$. Between sample and detectors we placed an evacuated beampipe.

5. Results

Both at the ESRF and at the APS we recorded time-correlation spectra at several angles $\delta\Theta$, including the one expected from equation (2). A typical recording time was 3 h. Fig. 4 shows a time-correlation spectrum, recorded at the detuning angle $\delta\Theta = 0.0217°$ for which maximum conversion is expected (with $\alpha_i = \alpha_s = 1.37°$). For compar-

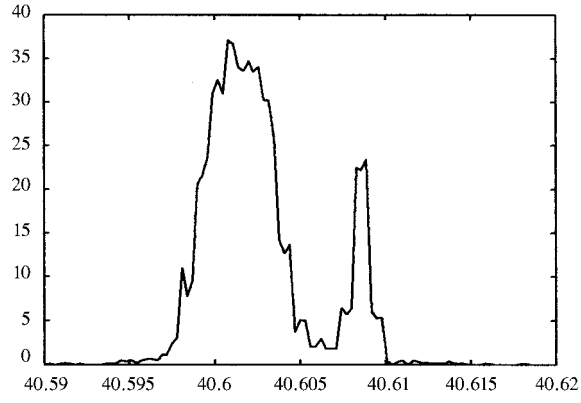

Figure 3
A rocking curve of the (400) diamond reflex, monitor corrected and scaled to show the true peak count rate. The abscissa shows degrees, the ordinate shows intensity in arbitrary units.

ison, Fig. 5 shows a spectrum recorded under identical conditions except for $\delta\Theta = -0.0217^\circ$ which is far off the phase-matching condition. By integrating over a range of ± 100 ns (corresponding to the detector time resolution) and subtracting the average over all of the time-correlation spectrum with the central region excluded, the number of coincidence events above the statistical level can be determined. Fig. 6 shows this rate for all detuning angles attempted at the ESRF. It shows that, indeed, the conversion rate peaks at the expected detuning angle. The width of this peak is not determined by the rocking width of the sample but rather by the size of the detector entrance windows because of the ensuing range $\Delta\alpha_{i,s}$ of the angles $\alpha_{i,s}$. Using equation (2) we obtain for the width $\Delta(\Delta\Theta) = \alpha_s \Delta\alpha_s / 2 \sin 2\Theta$, which in our case is calculated to be $\sim 0.002^\circ$.

As a cross check we recorded one time-correlation spectrum under the same conditions as in a real measurement, including the beam in the hutch, except with the detector entrance windows covered with lead. No correlations were recorded in this spectrum.

Owing to the lower flux at APS-1BM-C, single time-correlation spectra of the events in the drift-chamber detectors, each covering 1.5 h, show only weakly discernible coincidence peaks. Only the sum of all 12 time-correlation spectra recorded within 0.0003° of the detuning angle for maximum conversion exhibits a clear peak, seen in Fig. 7 and containing a total of 25 events. It is shifted away from zero time difference by 350 ns due to a coaxial cable delay in the preamplifier output of detector A, introduced to separate the true coincidences from any false ones which might be caused by common mode coupling of electronic noise into both signal-processing chains. In fact, there is no indication of such false events in the spectra. The time-correlation spectra recorded at other detuning angles show no coincidence peak.

At the APS we also recorded several time-correlation spectra with $\Delta\Theta$ set to maximum conversion rate but the Bragg reflected beam accidentally off the line through the centres of the two detector entrance windows by 2.5 mm. Thus, the condition that the wavevectors of the converted photons and of the Bragg reflected beam all be coplanar was violated. As is to be expected, these spectra do not exhibit a coincidence peak.

The avalanche diodes used at the APS provided no conclusive result because, both due to their larger active areas and their lack of energy resolution, the statistical event rates were fairly large.

6. Discussion

As stated above, an optimum choice of detectors for XPDC requires weighing the time and energy resolution in conjunction with the source time structure. If the synchrotron radiation source is filled very evenly [as in the experiment of Yoda *et al.* (1998)], avalanche photodiodes are a good choice and the Si drift chambers would probably perform approximately equally well, making up for inferior time resolution by superior energy resolution. At the ESRF in its two-thirds filling mode the high time resolution of avalanche photodiodes (APDs) may still be exploited. At the APS, operating in its current standard filling pattern, APDs cannot bring their time resolution to bear, making detectors like the Si drift chambers a better choice. In fact, the bunch spacings of 200 ns and 150 ns are well adapted to their time resolution, being approximately 100 ns.

In estimating the reduction in statistical background by use of the Si drift chambers, one should not be misled by the stated value of the energy resolution. The shape of an energy spectrum with monochromatic illumination is not at all Gaussian. Rather, there is a line of the stated width with a tail extending all the way down to zero energy. Within the stated linewidth, this tail contains $\sim 1\%$ of the integrated intensity in the line.

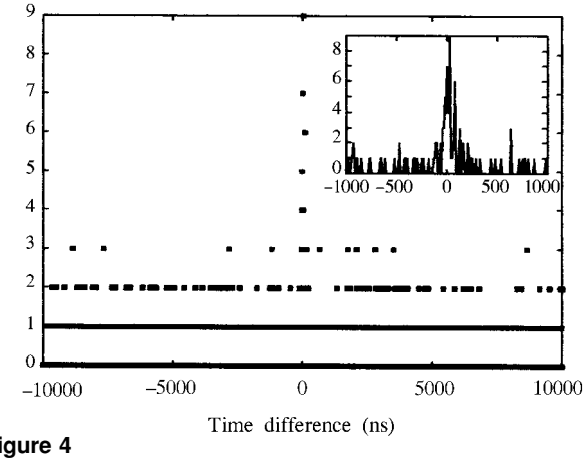

Figure 4
Time-correlation spectrum at $\delta\Theta = 0.0217^\circ$ (expected maximum conversion rate). The abscissa shows the time difference between the two detectors in ns over a range ± 10 μs and the ordinate shows the number of events in 3 h. There is a total of 46 events in 3 h. The inset is a zoom of the central ± 1 μs.

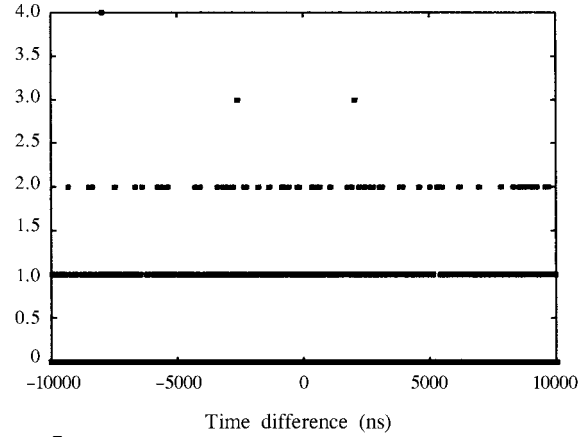

Figure 5
Time-correlation spectrum at $\delta\Theta = -0.0217^\circ$ (no conversion expected). The abscissa shows the time difference (ns). Abscissa and ordinate same as in Fig. 4.

We note that Fig. 7 shows a signal-to-background ratio which is considerably better than in Fig. 4. This is due to the tenfold lower incident intensity at the APS. Upon close inspection of Figs. 4 and 7, the coincidence peak in Fig. 7 seems to be wider. This effect may be due to the fact that the drift times in the detectors depend on the distance of the point where the photon is absorbed from the centre where the charge is collected. Owing to the rather small cross section of the incident beam at the ESRF, only small parts of the active detector areas would be hit by converted photons. This would give a spread of drift time differences which was smaller than at full illumination of the detectors, such as at the APS where the cross section of the incident beam was rather large.

To summarize the novel features of the experiments presented here, we used detectors which emphasized energy over time resolution for reasons discussed above. Instead of coincidences we recorded time-correlation spectra. Thereby, we had a direct comparison of the coincidence signal to the statistical background, covering about ± 3 periods of the ring period, *i.e.* several statistically equivalent points to statistical coincidence, as explained in §3.

7. Comparison with previous results

We now compare the event rates seen by us with those reported by Yoda *et al.* (1998) from the experiments at the Photon Factory. They show data from diamond (400) and (111) reflexes, taken with 19.1 keV incident energy and incident fluxes of 2.5×10^9 and 2.1×10^9 photons s^{-1}, respectively. The APD detectors, each with an active area of 5 mm^2 and estimated 60% quantum efficiency, were arranged at $\alpha_i = \alpha_s = 1.47^\circ$ and $\alpha_i = \alpha_s = 0.45^\circ$. Since a coincidence requires a response from both detectors, the quantum efficiency of 60% translates into ~36% coincidence detection efficiency.

Owing to the detuning from the Bragg angle, the extinction depth is much larger than the crystal thickness of 0.5 mm in both our experiment and that of Yoda *et al.* (1998). The effective thickness is obtained by dividing the crystal thickness by $\sin\Theta$. Our detectors have active areas of ~1.5 mm^2, *i.e.* slightly less than one-third of the APDs used by Yoda *et al.* (1998), and a quantum efficiency of close to 100% at the energies of the converted photons, resulting in close to 100% coincidence detection efficiency.

Because of the factor k_p^2 in equation (1), the conversion cross section per electron for the ESRF experiment is expected to be $(14.4/19.1)^2 = 57\%$ of that encountered by Yoda *et al.* (1998). The apex angle of the cone on which the converted photons exit was slightly smaller at the ESRF (1.37° as compared with 1.47°), resulting in a proportionally slightly larger expectation for the detected event rate.

With this information we can now compare the maximum event rate of 6 h^{-1}, reported by Yoda *et al.* (1998), with the 15 h^{-1} at the ESRF. At the ESRF we had a maximum of 2.5 times as many events per hour at six times the incident flux, 57% of the conversion cross section, about three-quarters of the effective crystal thickness, about one-third of the detector area and three times higher coincidence detection efficiency. The agreement is therefore quite good. A similar consideration for the APS data with a rate of 25 events in 18 h gives an agreement to within an order of magnitude.

A quantitative comparison of the theoretical expectation by equation (1) with the measured rates would require a detailed accounting of energy bandwidths, geometry factors, scattering form factors *etc.* In a very rough estimate we set $\gamma = 1$ in equation (1) and ignore scattering form

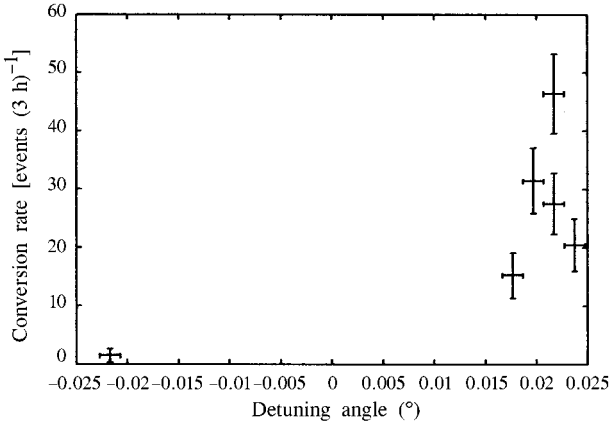

Figure 6
Background-corrected conversion rate in events per 3 h *versus* detuning angle. The maximum event rate is expected at $\Delta\Theta = 0.0217^\circ$. Two measurements were performed at that angle. The error bars show $\pm$(number of events)$^{1/2}$ in the vertical and 0.001° in the horizontal direction for counting statistics and estimated thermal drift of the equipment.

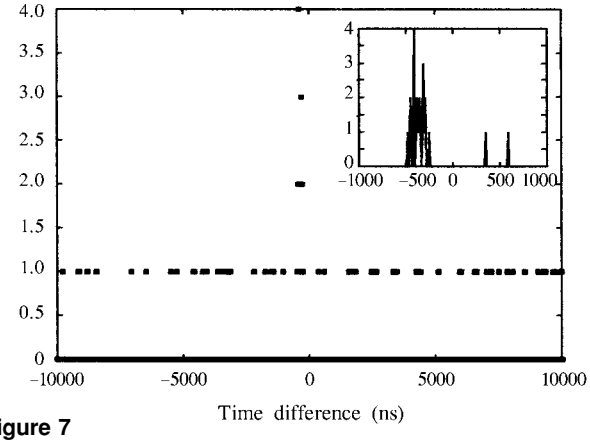

Figure 7
Sum of several time-correlation spectra all at the detuning angle for maximum conversion rate. The abscissa shows the time difference (ns) between detectors A and B. The coincidence peak is shifted to the negative because a delay of 350 ns (~60 m of coaxial cable) was introduced into the signal line from detector A (see text). The peak contains 25 events, collected in 18 h. The inset is a zoom of the central ± 1 μs. Abscissa and ordinate same as in Fig. 4.

factors. We also ignore dynamical diffraction effects, meaning that we just sum up the conversion cross sections of all electrons in the sample to obtain the total conversion rate. At 14.4 keV incident energy the conversion cross section of one electron into energy bandwidth $dx = 0.01$ is, according to equation (1), $d\sigma/d\Omega \simeq 6 \times 10^{-38}\,m^2$. Since a 1 mm-thick plate of diamond (*i.e.* 0.5 mm physical thickness divided by $\sin\Theta \simeq 0.48$) contains about 1×10^{27} electrons m^{-2}, there should be of the order of 6×10^{-1} conversions per second at an incident flux of 1×10^{10}, going into the whole cone around the reflected beam. Of this cone the Si drift-chamber detectors intersected ~3% in the ESRF experiment, so that we estimate an observable event rate of $\sim 2 \times 10^{-2}$ events per second. In view of the drastic simplifications in this estimate, it is of course purely by chance that the observed rate of one event in 240 s agrees so well with this estimate.

8. Conclusion and outlook

After the initial demonstration of XPDC by Eisenberger & McCall (1971), no further experimental results were published until those by Yoda *et al.* (1998). This is probably due to the weakness of the effect, requiring some experimental effort and offering little hope of practical applications of the correlated photons. Only with modern synchrotron radiation sources is it possible to obtain results within a few days of beam time. Quantitative measurements of conversion cross section, dependence on scattering conditions *etc.* are now within reach. On one of the proposed fourth-generation sources, such as the TESLA FEL (Brinkmann *et al.*, 1997), offering average brightnesses in the hard X-ray regime of up to four orders of magnitude more than currently available, it may even become possible to exploit the unique characteristics of the correlated photon pairs generated by PDC as a research tool. One field of application would be quantum optics, such as tests of Bell's inequality. In all these experiments the quantum efficiency of the detectors is of crucial importance. Both a lack of detection probability and a dark count rate essentially destroy the pure quantum state under investigation and mix it with external degrees of freedom. Despite great efforts, the maximum quantum efficiency reached to date for optical photons is ~70% (Kwiat, Steinberg, Chiao, Eberhard & Petroff, 1993) which is barely sufficient to detect a violation of Bell's inequality. Because X-ray detectors can achieve quantum efficiencies close to 100%, XPDC offers the perspective of so-called loophole-free tests of Bell's inequality.

Another interesting application of the pairs of correlated X-ray photons from XPDC would be the suppression of Poisson statistics in absorption spectroscopy (Adams, 1999). In a typical set-up, part of the intensity from the source is diverted for reference purposes, either by a scattering foil or by absorption in an ion chamber. For fundamental reasons the intensity incident on the sample is then known only within Poisson statistics. With pairs of correlated photons, one of each pair can go to a reference detector and the other one to the sample. The number of photons incident on the sample is thus exactly known. A typical application would be absorption spectroscopy of a trace element in a biological sample. In standard absorption spectroscopy a huge and possibly destructive radiation dose is required to discriminate the weak absorption signal from the statistics in the incident beam. The use of correlated photons would allow a drastic reduction of the radiation dose to the level required for discrimination of the absorption signal from the Poisson statistics of the absorption process itself, being relatively small in the case of a trace element.

APPENDIX *A*
The conversion cross section

The conversion cross section can be obtained in a semi-classical calculation by inserting the power density of vacuum fluctuations into the leading non-linear contribution to the electrical polarizability of free electrons. The derivation of the non-linearity is similar to one given by Eisenberger & McCall (1971). We begin with a multimode plane-wave electromagnetic field,

$$\mathbf{E}(\mathbf{r}, t) = \tfrac{1}{2}\textstyle\sum_j \mathbf{E}_j(\mathbf{r}, t),$$

$$\mathbf{B}(\mathbf{r}, t) = (c/2)\textstyle\sum_j \big[\mathbf{k}_j \times \mathbf{E}_j(\mathbf{r}, t)\big]/\omega_j,$$

with

$$\mathbf{E}_j(\mathbf{r}, t) = \mathbf{E}_j\big[\exp(i\mathbf{k}_j.\mathbf{r} - \omega_j t) + \text{cc}\big], \tag{3}$$

where cc means the complex conjugate of the immediately preceding term. The current density, $\mathbf{J}(\mathbf{r}, t) = \mathbf{v}(\mathbf{r}, t)\rho(\mathbf{r}, t)$, produced by these fields emits radiation at the frequencies of the incident fields and, by non-linear contributions, at sum and difference frequencies. If evaluated up to the second order, $\mathbf{J}$ can be written as $\mathbf{J}^{(1)}(\mathbf{r}, t) + \mathbf{J}^{(2)}(\mathbf{r}, t)$ with

$$\begin{aligned}\mathbf{J}^{(1)}(\mathbf{r}, t) &= \mathbf{v}^{(1)}(\mathbf{r}, t)\rho(\mathbf{r}) \\ \mathbf{J}^{(2)}(\mathbf{r}, t) &= \mathbf{v}^{(2)}(\mathbf{r}, t)\rho(\mathbf{r}) \\ &\quad + \mathbf{v}^{(1)}(\mathbf{r}, t)\big\{\rho\big[\mathbf{r} + \mathbf{x}^{(1)}(\mathbf{r}, t)\big] - \rho(\mathbf{r})\big\},\end{aligned} \tag{4}$$

where $\mathbf{x}^{(1)}(\mathbf{r}, t)$, $\mathbf{v}^{(1)}(\mathbf{r}, t)$ and $\mathbf{v}^{(2)}(\mathbf{r}, t)$ are the oscillation amplitude in the first order and the oscillation velocity in the first and second order, respectively, of a charge which is located at position $\mathbf{r}$.

There are three contributions to the second order, caused by the following effects: electrons which are oscillating in the above fields (i) sample the fields at positions other than their rest position and have non-zero velocities, giving rise to (ii) a non-linear Doppler shift and (iii) a non-linear Lorentz force.

The quantities $\mathbf{v}^{(1)}$, $\mathbf{x}^{(1)}$ and $\mathbf{v}^{(2)}$ may be determined by iteration of the Lorentz equation,

$$\dot{\mathbf{v}}(\mathbf{r}, t) = -\frac{e}{m}\left[\mathbf{E}(\mathbf{r}, t) + \frac{\mathbf{v}(\mathbf{r}, t) \times \mathbf{B}(\mathbf{r}, t)}{c}\right]. \tag{5}$$

In the first order this reads simply $\dot{\mathbf{v}} = -e\mathbf{E}/m$, so that

$$\mathbf{v}^{(1)}(\mathbf{r}, t) = -i\frac{e}{2m}\sum_j \frac{\mathbf{E}_j \exp[i(\mathbf{k}_j.\mathbf{r} - \omega_j t)] - \text{cc}}{\omega_j},$$

$$\mathbf{x}^{(1)}(\mathbf{r}, t) = \frac{e}{2m}\sum_j \frac{\mathbf{E}_j \exp[i(\mathbf{k}_j.\mathbf{r} - \omega_j t)] + \text{cc}}{\omega_j^2}. \quad (6)$$

Up to the second order the Lorentz equation reads now

$$\dot{\mathbf{v}}^{(1)}(\mathbf{r}, t) + \dot{\mathbf{v}}^{(2)}(\mathbf{r}, t) = -\frac{e}{m}\left\{\mathbf{E}\left[\mathbf{r} + \mathbf{x}^{(1)}, t\right] + \sum_j \mathbf{v}^{(1)}(\mathbf{r}, t) \times \frac{\mathbf{k}_j \times \mathbf{E}_j(\mathbf{r}, t)}{2\omega_j}\right\}, \quad (7)$$

where $\mathbf{B}$ has been expressed in terms of $\mathbf{E}$ by equation (3).

With the Taylor expansion

$$\mathbf{E}\left[\mathbf{r} + \mathbf{x}^{(1)}, t\right] = \mathbf{E}(\mathbf{r}, t) + (i/2)\textstyle\sum_j\left[\mathbf{k}_j.\mathbf{x}^{(1)}\right] \times (\mathbf{E}_j/2)\left\{\exp\left[i(\mathbf{k}_j.\mathbf{r} - \omega_j t)\right] - \text{cc}\right\}, \quad (8)$$

into which (6) can be inserted for $\mathbf{x}^{(1)}$ and, with (6) for $\mathbf{v}^{(1)}$, equation (7) is expressed in terms of $\mathbf{E}_j$, $\mathbf{k}_j$ and ω_j only. Except for the term $\mathbf{E}(\mathbf{r}, t)$ in the above Taylor expansion, everything belongs to the second-order acceleration,

$$\dot{\mathbf{v}}^{(2)} = -\frac{ie^2}{4m^2}\sum_{jj's}\left[\frac{\pm(\mathbf{k}_j.\mathbf{E}_{j'})\mathbf{E}_j}{2\omega_{j'}^2} - \frac{\mathbf{E}_{j'} \times \mathbf{k}_j \times \mathbf{E}_j}{\omega_{j'}\omega_j}\right] \times\left(\exp\left\{i\left[(\mathbf{k}_{j'} \pm \mathbf{k}_j).\mathbf{r} - (\omega_{j'} \pm \omega_j)t\right]\right\} - \text{cc}\right), \quad (9)$$

where the symbol s under the sum means that the sum runs over both cases '+' and '−' of $\pm$.

The contribution to the second-order current is

$$\mathbf{v}^{(2)}\rho(\mathbf{r}) = \frac{e^2}{4m^2}\sum_{jj's}\left[\frac{\pm(\mathbf{k}_j.\mathbf{E}_{j'})\mathbf{E}_j}{2\omega_{j'}^2(\omega_{j'} \pm \omega_j)} - \frac{\mathbf{E}_{j'} \times \mathbf{k}_j \times \mathbf{E}_j}{\omega_{j'}\omega_j(\omega_{j'} \pm \omega_j)}\right] \times\left(\exp\left\{i\left[(\mathbf{k}_{j'} \pm \mathbf{k}_j).\mathbf{r} - (\omega_{j'} \pm \omega_j)t\right]\right\} - \text{cc}\right) \times\rho(\mathbf{r}). \quad (10)$$

The other contribution to the second-order current density (5) comes from the term $\mathbf{v}^{(1)}\{\rho[\mathbf{r} + \mathbf{x}^{(1)}] - \rho(\mathbf{r})\}$ which can be expressed as $\mathbf{v}^{(1)}[\mathbf{x}^{(1)}.(\nabla\rho)(\mathbf{r})]$ by a Taylor expansion of ρ,

$$-i\frac{e^2}{4m^2}\sum_{jj's}\frac{\mathbf{E}_{j'}[\mathbf{E}_j.(\nabla\rho)(\mathbf{r})]\left\{e^{i[(\mathbf{k}_{j'} \pm \mathbf{k}_j).\mathbf{r} - (\omega_{j'} \pm \omega_j)t]} - \text{cc}\right\}}{\omega_{j'}\omega_j^2}. \quad (11)$$

The far-field expression for the electric amplitude $\mathbf{E}_s(\mathbf{r})$ from one oscillating electron at the coordinate origin is obtained by use of equations (9.13), (9.14), (9.17) and (9.19) of Jackson (1975):

$$|\mathbf{E}_s(\mathbf{r})| = (\omega_s/|\mathbf{r}|c^2)\left|\int \mathbf{J}^{(2)}(\mathbf{r}')\ \mathrm{d}\mathbf{r}'\right|, \quad (12)$$

with the domain of integration restricted to a region close to the origin.

For parametric down conversion from an incident plane wave $(\mathbf{k}_p, \omega_p)$ to two plane waves $(\mathbf{k}_i, \omega_i)$ and $(\mathbf{k}_s, \omega_s)$, only four terms in each of the sums over j, j', s in (10) and (11) are relevant. These are the ones in which the pump and signal or pump and idler waves have the indices j and j' or j' and j. These cases are all of the same order of magnitude and do not interfere destructively. As we are interested only in an order-of-magnitude estimate, we put the different vectorial products and the different frequency dependencies of the two terms in (10) and in (11) into a geometry factor γ which is of the order of unity. The vectorial factors $\mathbf{k}_j$ in the denominators of (10) then cancel each with one factor ω_j in the denominators (leaving $1/c$). In (11) there is $\nabla\rho$ instead of $\mathbf{k}_j$ in the denominator. For charges which are localized within much less than an X-ray wavelength, $\mathbf{E}_j.\nabla\rho$ times the complex exponential almost vanishes in the integration in (12) and, for more delocalized charges, $\nabla\rho$ is of the order of or less than an X-ray wavevector. We conclude that the contribution of (11) is of the same order of or even smaller than that of (10). With these order-of-magnitude estimates, we write (12) simply as

$$|\mathbf{E}_s(\mathbf{r})| = \gamma\frac{cr_e^2}{4e|\mathbf{r}|\omega_p}|\mathbf{E}_p||\mathbf{E}_i|, \quad (13)$$

with $r_e = e^2/mc^2$.

The energy of the radiant electromagnetic field with electrical peak amplitude $\mathbf{E}$ in a volume V is $\mathcal{E} = V|\mathbf{E}|^2/8\pi$ by equation (6.112) of Jackson (1975) and by the fact that the volume integrals over $|\mathbf{E}(\mathbf{r})|^2$ and $|\mathbf{B}(\mathbf{r})|^2$ are each equal to $V|\mathbf{E}|^2$. It can be related to the photon flux (number N of photons per time $\mathrm{d}t$ and area $\mathrm{d}\sigma$) at frequency ω by

$$\Phi = \frac{\mathrm{d}N}{\mathrm{d}t\mathrm{d}\sigma} = \frac{c|\mathbf{E}|^2}{8\pi\hbar\omega}. \quad (14)$$

Now, we take the square of (13) and replace $|\mathbf{E}_p|^2$ and $|\mathbf{E}_s|^2$ by the fluxes Φ_p of the pump and Φ_s of the signal, respectively,

$$\Phi_s = \gamma^2\frac{r_e^4c^2\omega_p}{16|\mathbf{r}|^2e^2\omega_s^3}\Phi_p|\mathbf{E}_i|^2. \quad (15)$$

So far the derivation has been entirely classical. In a semiclassical argument the field $\mathbf{E}_i$ is now given by the vacuum fluctuations and drives the spontaneous down conversion of X-ray photons. $|\mathbf{E}_i|^2$ is determined by the requirement that each mode at frequency ω in an arbitrary quantization volume V carries the energy $\hbar\omega/2$. Because the quantization condition of the wavenumbers for a linear dimension x is $kx = n\pi$ with integer n, each mode occupies a phase space volume of π^3. With $\mathcal{E} = V|\mathbf{E}|^2/8\pi$ for the radiant electromagnetic energy in a volume V, we have thus for the electric field of one mode,

$$\frac{\mathrm{d}|\mathbf{E}|^2}{\mathrm{d}\Pi} = \frac{1}{\pi^3}\frac{\hbar\omega}{2}\frac{8\pi}{V} = \frac{4\hbar\omega}{\pi^2V}, \quad (16)$$

where Π is the phase space volume.

The density of modes can be deduced by determining which volume in phase space (in coordinates k, x) is covered by an infinitesimal change in k,

$$\frac{\mathrm{d}\Pi}{\mathrm{d}k} = 4\pi V k^2 \Rightarrow \frac{\mathrm{d}\Pi}{\mathrm{d}\omega} = \frac{4\pi V \omega^2}{c^3}. \quad (17)$$

The power density of the vacuum fluctuations per frequency interval can now be found by an average over the modes, using (16) and (17),

$$\frac{\mathrm{d}\langle|\mathbf{E}|^2\rangle}{\mathrm{d}\omega} = \frac{4\hbar\omega}{\pi^2 V}\frac{4\pi V\omega^2}{c^3} = \frac{16\hbar\omega^3}{\pi c^3}. \quad (18)$$

We convert (18) into the relative bandwidth $\mathrm{d}x = \mathrm{d}\omega/\omega$, divide by two to select the running waves going one way from the standing waves in the above considerations and insert this into (15),

$$\frac{\mathrm{d}\Phi_s}{\mathrm{d}x} = \gamma^2 \frac{137 r_e^4 \omega_p \omega_i^4}{2|\mathbf{r}|^2 \pi \omega_s^3 c^2}\Phi_p, \quad (19)$$

where $\hbar c = 137e^2$ was used.

In the present experiment, $\omega_i \simeq \omega_s$. With $\omega_p = ck_p$, we arrive at the final result for the conversion cross section,

$$\frac{\mathrm{d}\sigma}{\mathrm{d}\Omega} = \gamma^2 \frac{137}{4\pi} r_e^4 k_p^2 \, \mathrm{d}x. \quad (20)$$

We would like to acknowledge the experimental support from the staff of beamline ID18 at the ESRF, most of all Dr R. Rüffer.

References

Adams, B. (1999). *ICFA 17th Advanced Beam Dynamics Workshop on Advanced Light Sources*, 6–9 April 1999, APS, Argonne, IL, USA. (http://www.aps.anl.gov/conferences/FLSworkshop/proceedings/WG1.htm.)

Brendel, J., Mohler, E. & Martienssen, W. (1991). *Phys. Rev. Lett.* **66**, 1142–1145.

Brinkmann, R., Materlik, G., Rossbach, J., Schneider, J. R. & Wiik, B.-H. (1997). *Nucl. Instrum. Methods*, A**393**, 86–92.

Eisenberger, P. & McCall, S. L. (1971). *Phys. Rev. Lett.* **26**, 684–688.

Freund, I. & Levine, B. F. (1969). *Phys. Rev. Lett.* **23**, 854–857.

Friberg, S., Hong, C. K. & Mandel, L. (1985). *Phys. Rev. Lett.* **54**, 2011–2013.

Hong, C. K., Ou, Z. Y. & Mandel, L. (1987). *Phys. Rev. Lett.* **59**, 2044–2046.

Jackson, J. D. (1975). *Classical Electrodynamics.* New York: John Wiley & Sons.

Kwiat, P. G., Steinberg, A. M. & Chiao, R. Y. (1993). *Phys. Rev. A*, **47**, R2472–2475.

Kwiat, P. G., Steinberg, A. M., Chiao, R. Y., Eberhard, P. H. & Petroff, M. D. (1993). *Phys. Rev. A*, **48**, R867–870.

Ou, Z. Y. & Mandel, L. (1988). *Phys. Rev. Lett.* **61**, 54–57.

Rarity, J. G. & Tapster, P. R. (1990). *Phys. Rev. Lett.* **64**, 2495–2498.

Rüffer, R. & Chumakov, A. I. (1996). *Hyperfine Interact.* **97/98**, 589–604.

Yoda, Y., Suzuki, T., Zhang, X.-W., Hirano, K. & Kikuta, S. (1998). *J. Synchrotron Rad.* **5**, 980–982.